ISOCAM CVF photometry report

(SAI/2001-034/Rp)

Blommaert[1], J.A.D.L., Boulanger[2], F., Okumura[2], K.

September 4, 2001

1: ISO Data Centre, Astrophysics Division, ESA, Villafranca del Castillo, P.O. Box 50727, 28080 Madrid, Spain
2: Institut d'Astrophysique Spatiale, Université Paris XI, 91405 Orsay

Abstract

We present the calibration of the ISOCAM CVF *Spectral Response Function*, which is based on observations of standard stars. The overall RMS uncertainty in the SRF is about 3%. The main difficulty for the photometry is the presence of reflected light on the detector. We studied different ways for point source photometry and conclude that aperture photometry with radii are 6, 4, 3 for 1.5, 3 and 6$''$ PFOV respectively gives the best results. The background was taken in an annulus of 2 pixels wide around the aperture. *In order to minimize the photometric error on any ISOCAM astronomical CVF data, we recommend to use, as close as possible, the same photometry method as that adopted for the calibration.* The extended source calibration has been performed with the zodiacal light observations using the DIRBE model. The filter calibration agrees well with that of the point sources. For the CVFs we observe a systematic departure from point sources due to the impossibility of separating direct illumination from the stray light. We have combined zodiacal and point source observations to correct the zodiacal observations for stray light. The accuracy to which we can test the absolute photometry for extended sources is finally limited to about 10% by the accuracy of the DIRBE model. The ISOCAM data suggest the existence of a silicate feature not included in the model. We do not see any meaningful straylight correction for the CVF observations of extended sources with contrasted structure.

1 Introduction

In this report we describe the flux calibration of the ISOCAM Long Wavelength (LW) Circular Variable Filters (CVFs). The results of our analysis are used to derive the Spectral Response Function (SRF) for the Off Line Processing version 10 (OLP 10). The SRF is determined on basis of standard star observations. ISOCAM CVF is a powerful instrument allowing spectroscopy in a wide wavelength range (2-18 μm) for a region of $3' \times 3'$, but it is also a complicated one. A very careful analysis of the data is necessary to obtain good photometry. We will give an overview of different aspects which are important for photometry, like the presence of reflected light, the shape of the Point Spread Function (PSF). The report further includes the calibration of extended sources based on the zodiacal background measurements.

In Sect. 2 we discuss the observing method and data analysis of calibration star measurements. Different methods for deriving point source photometry are discussed in Sect. 3. In

Table 1: Stars used for the CVF calibration

Name	HIC	HR	HD	SAO	R.A. Dec.	Spec. Type
γ Draconis	87833	6705	164058	030653	17:56:36.37 +51:29:20.0	K5III
δ Draconis	94376	7310	180711	018222	19:12:33.30 +67:39:41.5	G9III
-	94890	7341	181597	048315	19:18:37.87 +49:34:10.0	K1III
-	96441	7469	185395	31815	19:36:26.54 +50:13:16.0	F4V
Sirius	32349	2491	48915	151881	06:45:08.92 −16:42:58.0	A0m

the subsequent section we discuss the stellar models to derive the SRF. Sect. 5 describes the obtained SRF and a comparison with the SRF available in earlier calibration files. The analysis of the zodiacal background is the subject of Sect. 6.

"*The ISOCAM CVF Calibration Report*" (Biviano et al. 1998 [2]) gives an overview of the general calibration through the CVFs. We still refer the reader to this report for other CVF issues than the LW photometry ones. The necessity of this work was felt due to the fact that the CVF SRFs in the earlier calibration files did not contain any error estimates and also that the photometry of a perfectly extended source had not been sufficiently analysed.

2 Stellar Observations

The SRF is derived from the observations of calibration stars. The stars were selected from samples provided by the Ground Based Preparatory Program (GBPP, Hammersley et al. 1998 [13], Hammersley & Jourdain de Muizon [14]) and by Martin Cohen (Cohen et al. 1999 [6] or Cohen 2001 [7]). A discussion of the Spectral Energy Distribution (SED) models of these stars is given in Sect. 4. In brightness range the stars span 2 orders of magnitude. In comparison to the ones selected for the filter calibration (Blommaert 1998, [4]), they are relatively bright because the band width on a segment of CVF is small compared to those of the large bandpass filters. Tab. 1 shows the sources used for the CVF calibration. Tab. 2 lists the observations used for the calibration. γ Draconis, δ Draconis and Sirius are relatively well known calibration stars which were also observed by other ISO instruments (Photometry Working Group Report, [5] and the ISO Cross Calibration Report, [12]).

The strategy followed the one used for the filter photometric calibration (Blommaert 1998 [4]). For reasons of time, most observations were performed in one single direction and not forth and back, as is recommended to be able to quantify transient effects. In the majority of the cases the scan starts at the shortest wavelengths where the sources are brightest.

2.1 Data reduction

All data analysis was performed within the CIA package [15]. The 'vilspa' method was used for the **dark correction** of all the data. This is the most recent method which takes into account the time and temperature dependencies of the dark current. For the present analysis, any dark current remnant has only marginally importance to the signal of the observed stars.

Table 2: CVF calibration related observations, The TDT numbers marked with * were used for the SRF determination

CVF	Wavelengths	Step	Lens	TDT No.	Target	Gain	Tint	Comments
LW1	9.583-5.446	4	1.5"	05804802	HIC94890	2	2.10	
LW1	9.583-4.956	1	3.0"	05804903	HIC94890	2	2.10	
LW1	9.583-5.446	4	6.0"	05805004	HIC94890	2	2.10	
LW2	16.70-9.003	4	1.5"	05805408	HIC94890	2	2.10	
LW2	16.70-8.782	1	3.0"	05805509	HIC94890	2	2.10	
LW2	16.70-9.003	4	6.0"	05805610	HIC94890	2	2.10	
LW1	9.583-4.956	1	3.0"	06200204*	HIC96441	2	2.10	
LW1	4.956-9.583	1	3.0"	06200305*	HIC96441	2	2.10	
LW2	17.34-8.782	1	3.0"	06200713*	HIC96441	2	2.10	
LW2	8.782-17.34	1	3.0"	06200814*	HIC96441	2	2.10	
SW	2.273-5.122	1	3.0"	06201222	HIC96441	2	2.10	
SW	5.122-2.273	1	3.0"	06201323	HIC96441	2	2.10	
LW1-	9.583-4.956	4	1.5"	06201502	δ Draconis	1	1.12	X-cal
-LW2-	17.34-8.893	4	1.5"	06201502	δ Draconis	1	1.12	X-cal
-SW	2.273-5.097	4	1.5"	06201502	δ Draconis	1	1.12	X-cal
LW1-	9.487-5.079	1	6.0"	06600401	Zodiacal	1	2.10	Extended
-LW2-	16.60-9.03	1	6.0"	06600401	Zodiacal	1	2.10	continued
-LW1-	5.070-9.438	1	6.0"	06600401	Zodiacal	1	2.10	continued
-LW2	9.03-16.60	1	6.0"	06600401	Zodiacal	1	2.10	continued
LW2	11.27-9.551-11.27	1	3.0"	06602001	NGC6543	2	2.10	
SW	2.273-4.996	4	6.0"	06602814	HIC94890	2	2.10	
SW	2.273-5.122	1	3.0"	06602915	HIC94890	2	2.10	
SW	2.273-4.996	4	1.5"	06603016	HIC94890	2	2.10	
LW1-	9.487-4.956	4	1.5"	07807002	δ Draconis	1	1.12	X-cal
-LW2-	17.34-8.893	4	1.5"	07807002	δ Draconis	1	1.12	X-cal
-SW	2.273-5.097	4	1.5"	07807002	δ Draconis	2	1.12	X-cal
LW1	4.956-9.583	1	3.0"	20305503*	δ Draconis	1	1.40	
LW2	9.003-16.52	1	3.0"	20305604*	δ Draconis	1	2.10	
LW2	9.003-16.52	1	1.5"	32800403*	δ Draconis	1	2.10	
LW1	4.956-9.583	1	1.5"	32800504*	δ Draconis	1	1.12	
LW2	8.782-16.52	1	6.0"	32800302*	δ Draconis	1	1.12	
LW1	4.956-9.583	1	6.0"	32800605*	δ Draconis	1	1.12	
LW2	8.782-16.52	1	3.0"	37000702*	δ Draconis	1	2.10	
LW1	4.956-9.583	1	3.0"	37000803*	δ Draconis	1	1.12	
LW1	6.511	0	6.0"	40600602	δ Draconis	1	1.12	no scan
LW1	6.511	0	3.0"	40600703	δ Draconis	1	1.12	no scan
LW1	6.511	0	1.5"	40600804	δ Draconis	1	1.12	no scan
SW	2.273-5.122	1	6.0"	40601802	HIC96441	1	2.10	
SW	5.122-2.273	1	1.5"	40601903	HIC96441	2	2.10	
LW2	9.003-16.52-9.003	2	1.5"	48206902	γ Draconis	1	1.12	
LW1-	5.018-9.438	4	6.0"	49600802	δ Draconis	1	1.12	bottom left
-LW2-	9.551-16.42	4	6.0"	49600802	δ Draconis	1	1.12	continued
-LW2-	16.42-9.551	4	6.0"	49600802	δ Draconis	1	1.12	continued
-LW1	9.487-5.079	4	6.0"	49600802	δ Draconis	1	1.12	continued
LW1-	5.018-9.438	4	6.0"	49600803	δ Draconis	1	1.12	bottom right
-LW2-	9.551-16.42	4	6.0"	49600803	δ Draconis	1	1.12	continued
-LW2-	16.42-9.551	4	6.0"	49600803	δ Draconis	1	1.12	continued
-LW1	9.438-5.018	4	6.0"	49600803	δ Draconis	1	1.12	continued
LW2	14.520-17.34-14.52	1	1.5"	80100702*	γ Draconis	1	1.12	
LW2-	17.34-8.782	1	1.5"	83901902*	Sirius	1	1.12	One block
-LW1-	8.993-6.684-8.993	1	1.5"	83901902*	Sirius	1	1.12	continued
-LW2	8.782-17.34	1	1.5"	83901902*	Sirius	1	1.12	continued

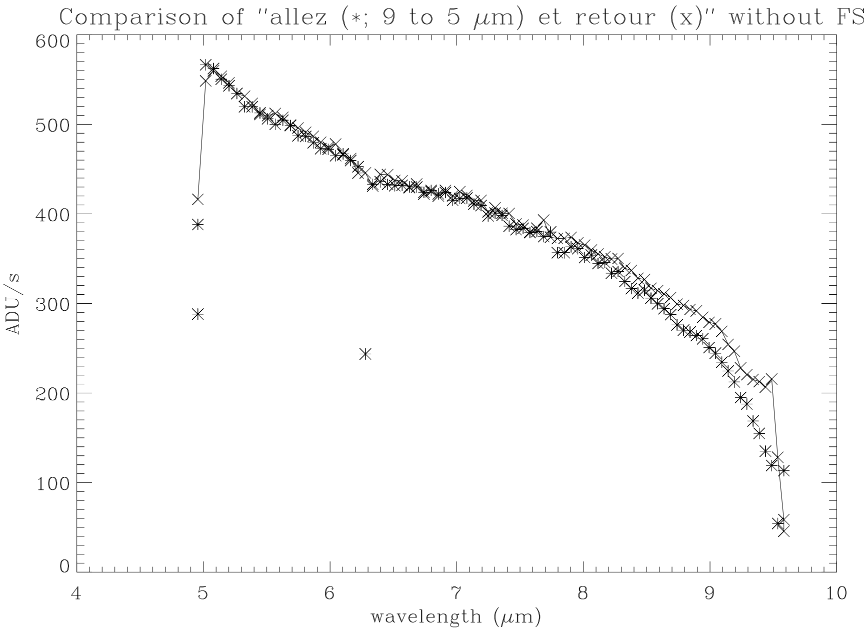

Figure 1: The for- and backward LW1 CVF scan of HIC096441 without FS application

The following step concerns **deglitching**. Several methods exist within CIA. Generally, *deglitch_MM* is considered the most successful although it is not always useful for bright sources (Biviano 1998 [3], Blommaert 1998 [4]). A good alternative for bright point sources like the ones observed for the calibration of the CVF is the method *deglitch_temp* which is applied on each individual cube per CVF step.

The last step exists of correcting the data for *transient* problems. For this the *'Fouks-Schubert'* (FS) method (Coulais and Abergel 2000 [8]) was used. This method was not developed for point sources. Nevertheless it is found that it can improve data on point sources as well, especially for weaker pixels in the wings of the PSF which stabilize slower. The method if not effective certainly does not harm the data. Also FS is applied in the OLP10 data reduction. For these reasons we decided to apply the method here as well. For the brightest sources observed, the effect of the FS method on the photometry is very small. In cases where the source is weaker (at the longest wavelengths for stars) like is the case for HIC096441, the correction becomes more important see Fig.1 and Fig. 2 where a comparison is given of the measurement without and with FS correction. To take out parts which were not corrected properly by FS we used *KSig* so that only values in the cube are kept which are close to the final value per CVF step. This algorithm selects the later part of the readouts within a given configuration by clipping the values which deviate more than twice the RMS from the mean value in each iteration.

An image is created for each CVF by averaging the valid points of the cube of measured readouts. The image is then *flatfielded* by dividing it by the *detector flatfield*. It was decided not to use the *optical flatfield* measured through the filter with the nearest wavelength, for it may be different from that of the CVFs. In addition, since the star is always measured in the centre of the array the effect of flatfielding is only minimal.

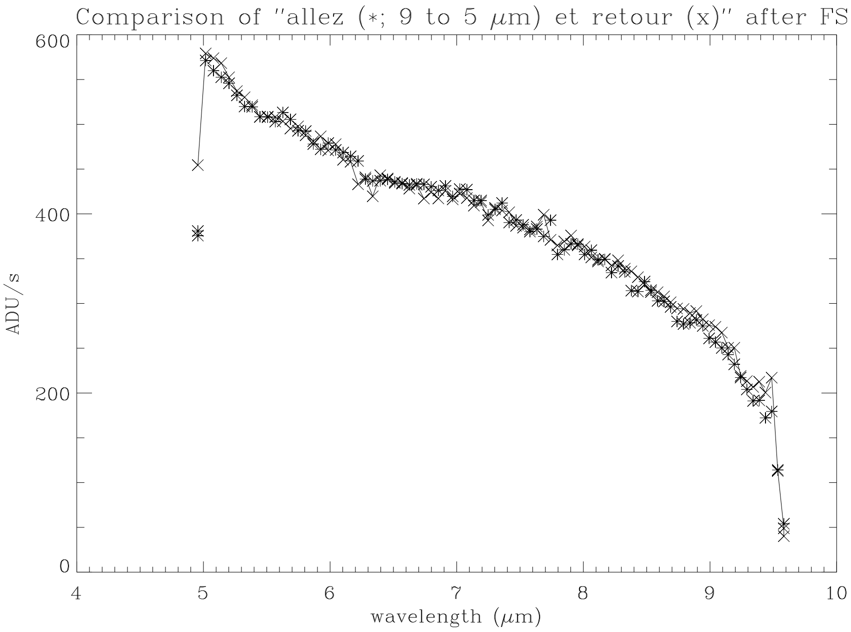

Figure 2: The for- and backward LW1 CVF scan of HIC096441 with FS application. The FS correction gives a better agreement at the longest wavelengths where the signal is lowest and where the measurement started.

3 Point Source Photometry

Different methods can be applied to measure the observed signal from a point source. One is to apply aperture photometry. To be independent of aperture size and to be able to make the absolute flux calibration also applicable on extended sources one needs to correct the aperture photometry for the part of the Point Source Function (PSF) outside the aperture. This was the method used for the absolute flux calibration of the filters (Blommaert 1998) and for the previous version of the SRF (Biviano et 1998). Another photometric method is fitting a PSF to the measured point source. Both methods will be discussed in the following subsections.

Some complication in the CVF photometry arises from the presence of reflected light on the array (Okumura 2000 [20]). Part of the reflected light falls back near and on the source and needs to be separated in the flux measurement. The so-called "ghost" contributions are also different for different lenses and thus complicate the comparison of the different PFOVs. An analysis of how the "ghost" can be treated for the photometry is explained below. In Section 3.2.3 a special method is presented based on the modelling of the ghost reflection.

3.1 PSF in the CVF measurements

We first describe in further detail the observed PSF for CVFs. For both the photometric methods they are essential. Obviously so for the psf-fitting method (see § 3.2.1), but also in the aperture photometry where a psf-correction is applied for the point source flux falling outside the aperture. A description of the theoretical PSFs is given in Okumura 2000 [20] and Okumura 2001 [21].

In Fig. 3 we see that the PSFs of the CVFs are wider than the computed ones. The same effect was already known to exist for the broad band filters (Okumura 1998 [19]) but only for

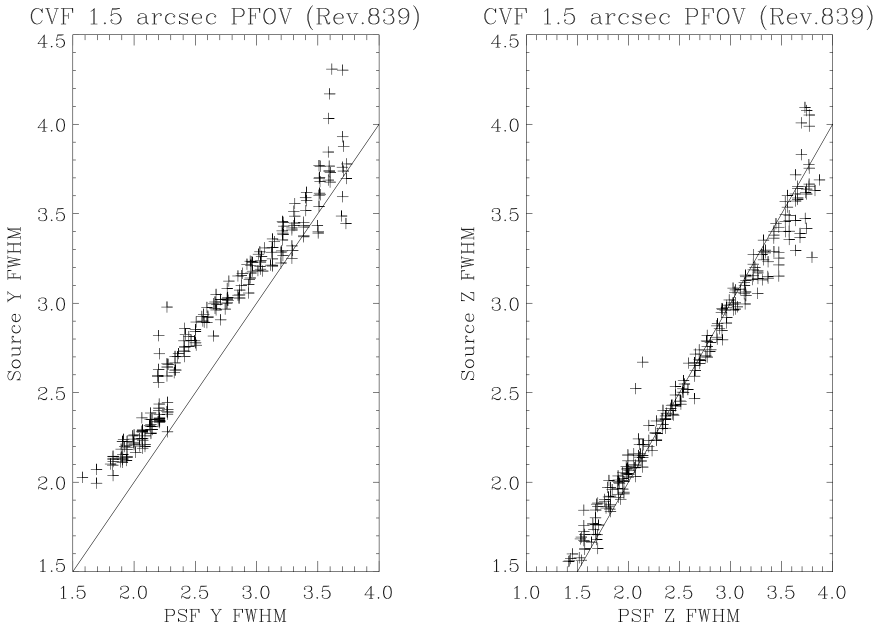

Figure 3: FWHM correlation in pixel units between a point source observed through the CVFs and one of the PSF models at different positions which provides the best match with the source

the shortest wavelengths ($< 7\mu$m). Furthermore, a clear discontinuity at 9 μm between the two CVF segments is present. In Fig. 3 the discrepancy shows up strongest for Full Width Half Maximum (FWHM) in the Y axis (horizontal in the CIA convention).

The discontinuity at 9 μm may suggest that the measured CVF PSF width is affected by the ghost flux which is wavelength dependent and changes abruptly between the two segments (see Fig. 25). However, the ghost contribution is negligible through the $1.5''$ PFOV lens (Okumura 1998 [19]), and it seems difficult to explain the CVF PSF anomaly only with the ghosts contribution. What causes the larger PSFs for the CVF is not understood.

3.2 Different methods of the point source photometry

3.2.1 PSF fit for different lenses

An alternative photometric method to the aperture one is to derive the flux by fitting the source with a PSF. A possible advantage of this method is that it may be less hampered by (an extended) ghost. In order to deal with under-sampled data, one PSF is selected among a set of PSFs located at different positions relative to the pixel center. The selection is based on the minimum deviation criteria between the PSF and a point source image. The linear fit of the selected PSF on the point source provides the flux and background level which is supposed to be flat.

The consequence of the deviation of the PSF width on the point source photometry is that the PSF fit program underestimates the flux compared to the aperture photometry. Figs. 4 and 5 show the ratio between these two fluxes for measurements through $1.5''$ PFOV lens. In the case of the broadband filters (Fig. 4) the flux determined with PSF-fit is underestimated with respect to the aperture photometry for wavelengths short-ward of 7 μm as could be expected

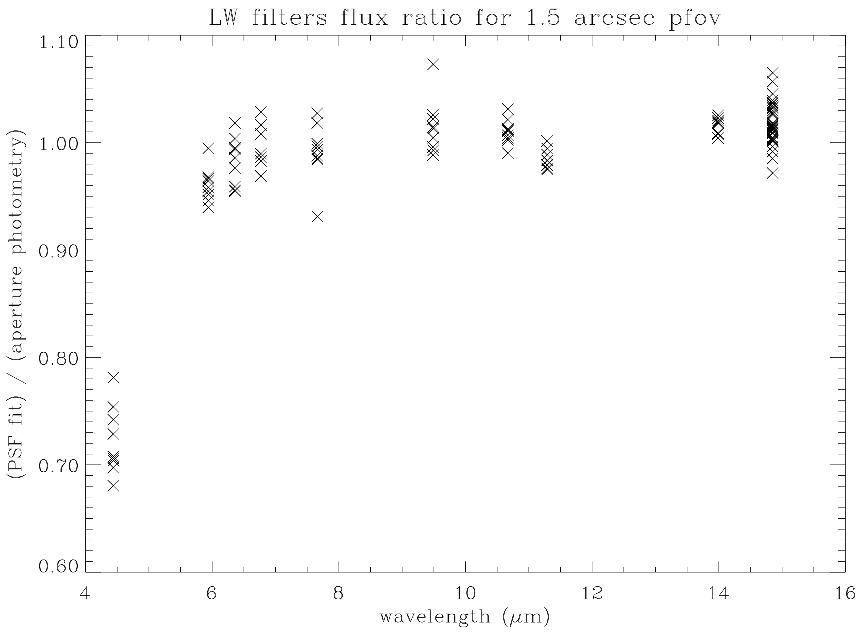

Figure 4: Ratio of PSF fit flux to aperture photometry flux for LW broad band filters through the 1.5″ pfov lens

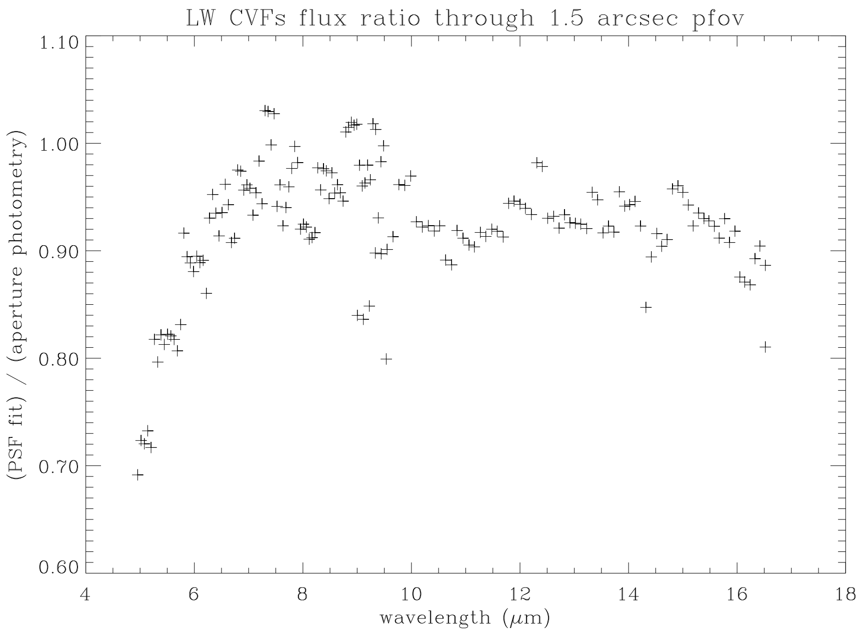

Figure 5: Ratio of PSF fit flux to aperture photometry flux for LW CVFs through the 1.5″ pfov lens

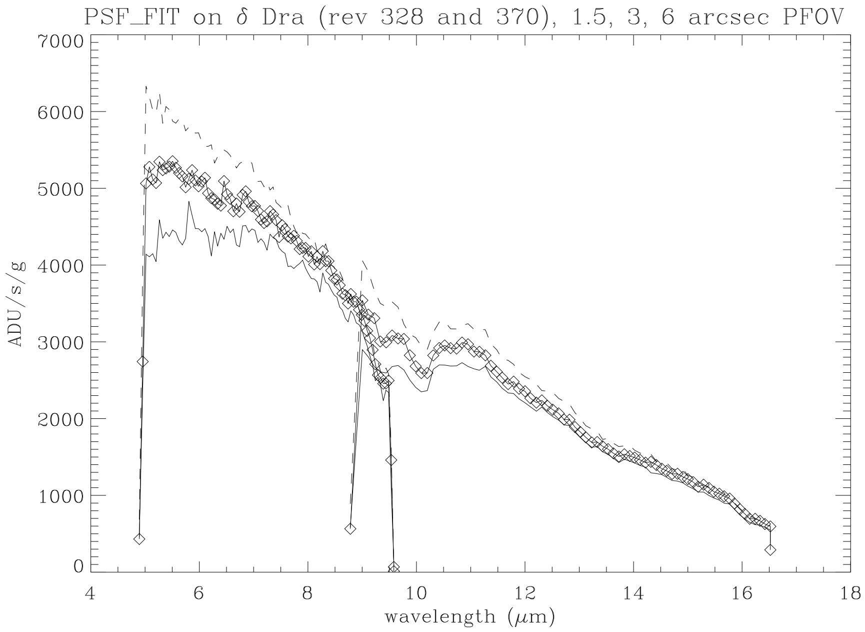

Figure 6: Photometry by applying PSF fit on three different PFOVs. The solid line represents 1.5″, the diamonds 3″ and the broken line 6″ PFOV.

from the discussion on the PSF sizes. As for the CVF, due to the fact that the theoretical PSF sizes are underestimated over a larger wavelength range, the ratio of the aperture over PSF-fit photometry is below unity over a large wavelength range and also the discontinuity at 9 μm between the two CVF segments is seen.

The flux discrepancy is strongest for the 1.5″ PFOV lens. For the larger PFOVs, due to the pixel convolution effect, the difference between the observed and modelled PSF becomes smaller and the flux discrepancy decreases. Fig. 6 gives a comparison of the flux derived for δ Dra observed on revolutions 328 and 370 with three different pixel field of views. The result is very different in the 3 cases with increasing differences going to shorter wavelengths for both CVF parts. As it is mentioned above, the theoretical PSF used to fit the observed source is not adequate and the deviation increases from 6 to 1.5″ PFOV.

3.2.2 Aperture photometry

With fixed filter measurements it was found that applying aperture photometry was giving the most stable results. This method however also depends on the knowledge of the PSF as one needs to correct for the part of the source falling outside the aperture. The freedom of choosing the aperture to be used on the CVF is limited by the presence of the ghost. This is well demonstrated in Fig. 7 where aperture photometry for different radii are compared on point sources measured with fixed filters and the CVF. For 6″ PFOV the CVF fluxes differ considerably from those obtained with the fixed filters which are more or less ghost free. For the smaller pixel measurements the CVF and filters are consistent. Different radii of the aperture give different results. This is explained by the fact that the theoretical PSF used for the correction and the observed one are not perfect matches. Especially at small radii, the differences can be important.

Using larger radii, one can still find differences up to 10%.

3.2.3 Ghost intensity measurements and source-ghost separation

The main difficulty for CVF point source photometry lies in the presence of the undesirable flux of ghosts. In the case that the point source is positioned well off-centre it is possible to judge the contribution of the ghost. We know from the ray tracing ghost simulation that the ghosts appear when multiple reflections occur between the detector and the filter surface. When the point source is at the detector center through the $6''$ pfov lens, the main and the secondary ghosts both sit on the source image and it is not straightforward to know the contribution of each flux and separate them. However there are observations made for calibration purposes which place a point source at two bottom corners of the detector (TDT No.49600802 and 49600803 in Tab. 2). In these cases, the main ghost still remains on the source image, whereas the secondary ghost is well separated and placed at the azimuthally symmetrical position of the source. The optical model shows that the secondary ghost is generated by twice the beam paths of the main ghost. This allows to determine the relationships between the fluxes assuming a global reflectivity of the intervening optical elements.

Let s be the flux of the point source, g that of the main ghost and h that of the secondary ghost. In the specific data, it is easy to measure the sum $S = s + g$ and h. The ratio $f = S/h$ is then directly computed. If α is the global reflectivity on the detector and the filter surface, and β the fraction of the main ghost flux on the detector, one can write :

$$
\begin{aligned}
g &= \alpha\beta s \\
h &= \alpha g = \alpha^2\beta s
\end{aligned}
$$

The parameter β is necessary because a part of the main ghost falls outside the detector in the data 49600802. Its value should be evaluated in a geometrical way. In the data 49600803 the main ghost is entirely on the detector which allows β to be considered as unity. The secondary ghost is never too close to the detector edge. The ratio f is then expressed as :

$$f = \frac{1+\alpha\beta}{\alpha^2\beta}$$

The global reflectivity is a positive root of the second order equation :

$$f\beta\alpha^2 - \beta\alpha - 1 = 0$$

The fluxes of the source and the main ghost can then be separated as :

$$
\begin{aligned}
\alpha &= \frac{1+\sqrt{1+4f/\beta}}{2f} \\
s &= \frac{h}{\alpha^2\beta} \\
g &= \alpha\beta s = \frac{h}{\alpha}
\end{aligned}
$$

In Fig. 8 a comparison of SRFs determined by different methods is shown. It shows that generally the normal aperture photometry and the method described in this subsection agree well.

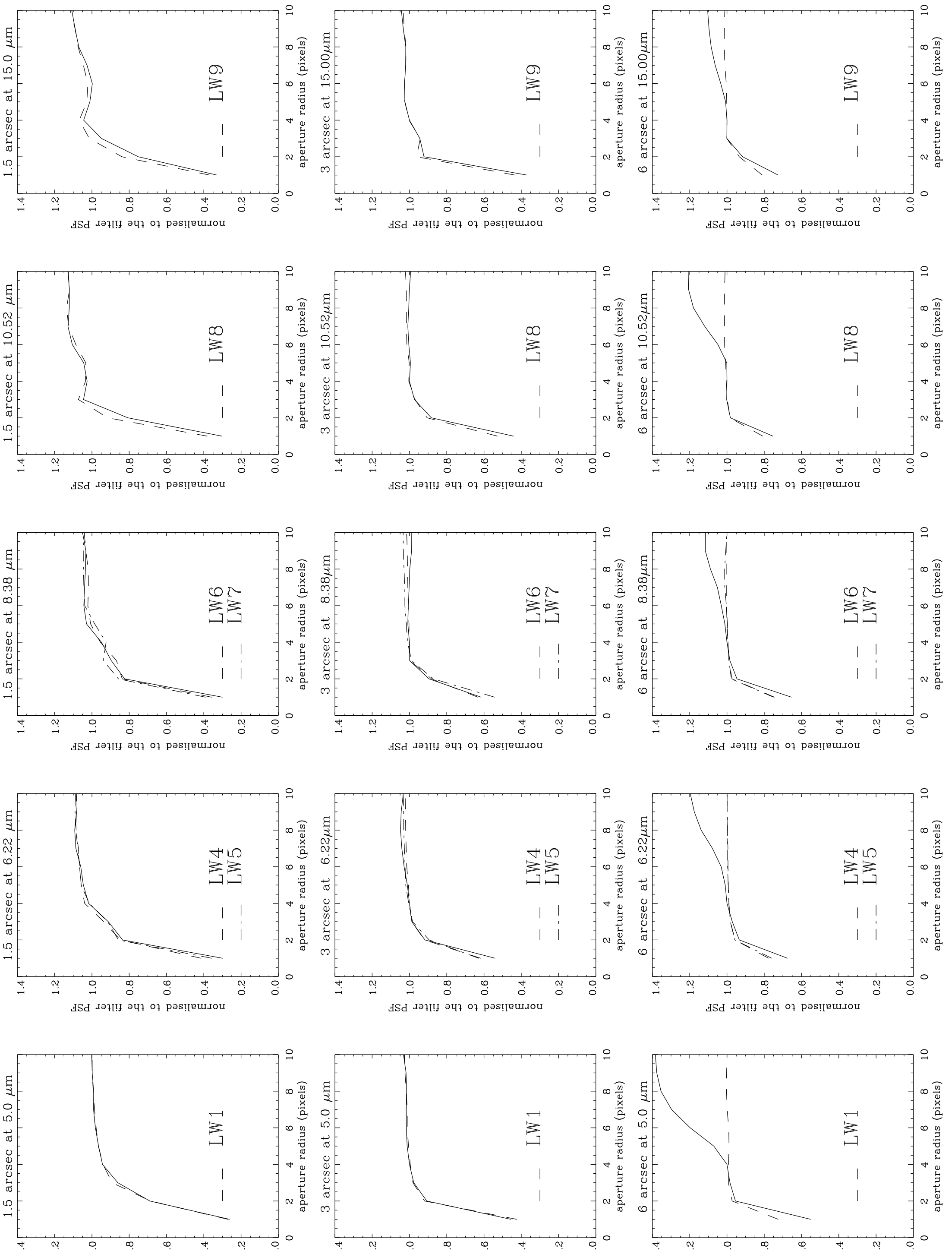

Figure 7: Aperture photometry with variable apertures showing the error caused by the aperture correction.

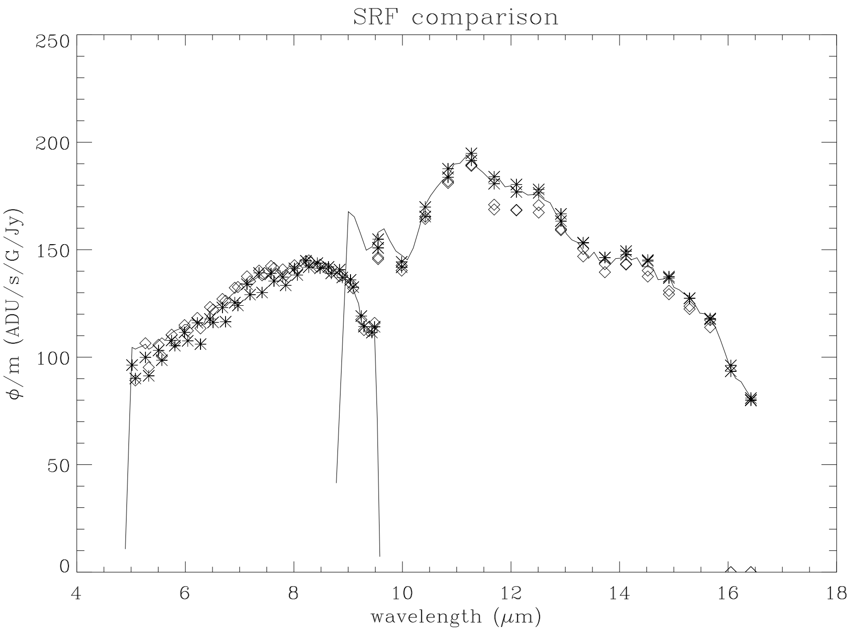

Figure 8: Comparison of the SRFs. Photometry by ghost separation with the source at bottom left corner (diamonds), aperture photometry on the same data (asterisks). Also shown is the aperture photometry on the same source γ Dra in the data 32800302 and 32800605 where the source is at the detector center (line).

3.3 Final photometry method used for Cal-G file

Considering the results described in the previous subsections, we opted for using aperture photometry. We choose the radii large enough not to underestimate the flux but avoiding inclusion of the ghost contribution (Fig. 7). The resulting radii are 6, 4, 3 for 1.5, 3 and $6''$ PFOV respectively. The background was taken in an annulus of 2 pixels wide around the aperture. In order to minimize the photometric error on any ISOCAM astronomical CVF data, it is recommended to use, as close as possible, the same photometry method as that adopted for the calibration measurement, although it is not always easy because of the source confusion in a crowded region of the sky.

4 The Stellar Models as input for the SRF

The stars observed for the CVF calibration have quite different stellar types (see Table 1). The spectra of the earlier type stars are dominated by atomic lines whereas molecular bands dominate the spectra of the cool stars (Decin 2001 [10]). Originally the calibration of ISOCAM was done by using stellar models provided by the Ground Based Preparatory Programme (Kurucz models fitted to visible and near-infrared data, Hammersley et al. 1998 [13], Hammersley & Jourdain de Muizon [14]) or the "Composites of observed spectra" (different observed spectra put together with photometric measurements) and "spectral templates" (composite spectrum of another star with similar stellar parameters, shifted to the visible and near-infrared photometric data available for the calibration star) provided by Cohen (Cohen et al. 1999 [6] or Cohen 2001 [7]). For more information on the stellar models see the Photometry Working Group Report,

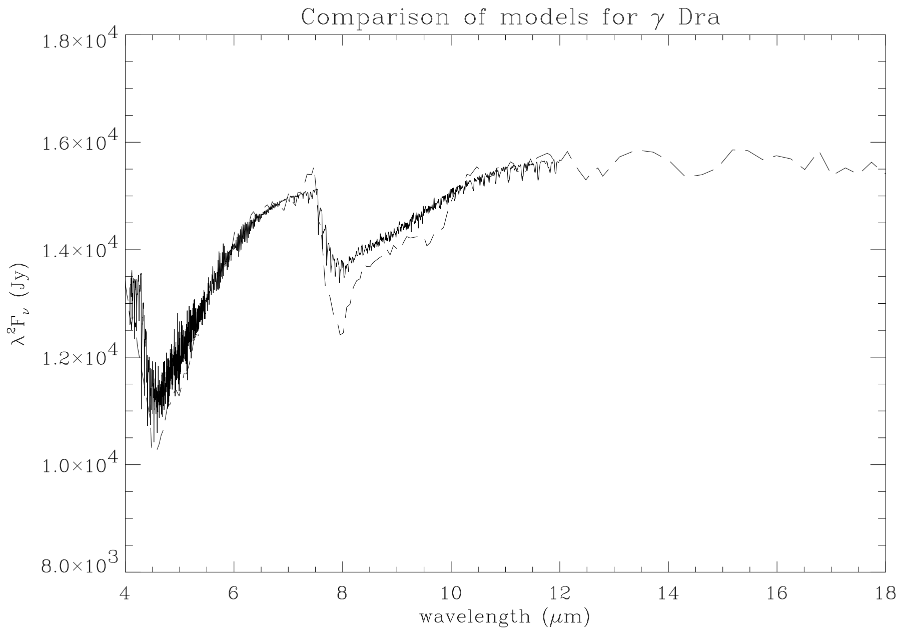

Figure 9: Comparison of the stellar composite in dashed line (Cohen) with the spectral model by Decin in solid line (2000) for γ Draconis

[5].

During the mission, Decin et al. 2000 [9] and Decin et al. 2001 [11] produced new model spectra based on a combination of state of the art existing synthetic spectra modelling and SWS observed spectra. For the calibration stars observed with the CVF, model spectra were available for γ Draconis (K5III), δ Draconis (G9III) and Sirius (A0m). The model spectra from Decin are absolute flux calibrated in the same way as the Cohen models and are thus connected to the Cohen Vega model. Note that the Decin models are only available up to 12 μm (the long wavelength limit of SWS band 2C).

Late spectral type stars contain molecular absorption band features which are not well modeled by the Kurucz models provided (the SiO fundamental around 8μm is for instance missing). In those cases we need to take the input spectra from either Decin or Cohen. Decin (2001) gives a comparison between her and Cohen's input spectra. Here we concentrate on the stars used for the CVF calibration. A comparison for γ Draconis, shows differences up to a few percent in the CO (around 5 μm) and fundamental SiO (around 8 μm) bands (Figure 9). Only the segment 2 was used of the CVF, so that the star was only observed at longer wavelengths than 9 μm where there are only little differences between the 2 models.

For δ Draconis, Cohen provides a stellar template, which is based on the composite spectrum of β Gem, a star which resembles δ Draconis, according to Cohen. Again some differences are found in the model provided by Decin and Cohen in the region of the molecular bands (Figure 10). Sirius showed little differences between the Cohen and Decin models, especially for the CAM CVF resolution and the wavelength range ($> 6.7\mu$m) in which Sirius was observed with CAM.

For HIC096441 (F4V) only a (Kurucz) model is available from the GBPP. For HR7341 (K1III) only a stellar template of Cohen was available. As there was no independent reliable model and there were sufficient measurements of the other four stars, we didn't use HR 7341 in

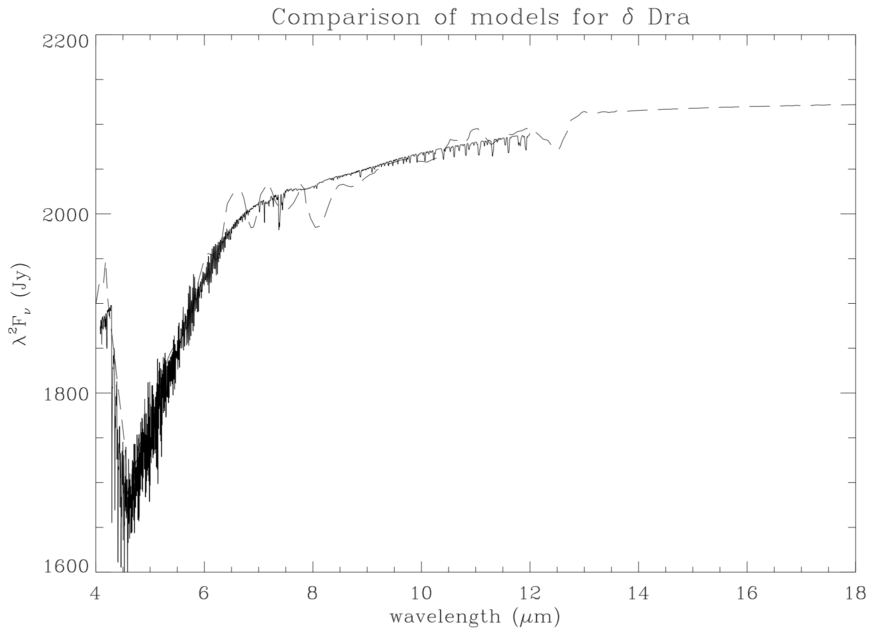

Figure 10: Comparison of the stellar template in dashed line (Cohen) with the spectral model by Decin in solid line (2000) for δ Draconis

the determination of the SRF, because of the uncertainty in the molecular bands. In Appendix A we compare the template with the observation using the new SRF.

The final calibration of the CVF measurements was done in analogy of the RSRF calibration of SWS (ISO Handbook Volume VI: SWS [16]). Up to 12μm, we use the model provided by Decin. For the longer wavelengths, Cohen was used. The combined models were smoothed to the resolution of the CAM CVF (~ 40). For HIC096441 simply the Kurucz model provided by the GBPP was applied.

5 The mean SRF

The SRF is determined from the observations indicated by an asterisk after the TDT number in Table 2. The other data in the Table have not been retained in the final result either because the signal to noise ratio is low or because the CVF scanning step is larger than 1. The latter data would have introduced a saw teeth structure in the averaged SRF. Four different stars of different flux levels were used: (Sirius, γ Draconis, δ Draconis and HIC096441). Observations of different PFOV and integration times are included. The mean SRF is the average of the independent SRFs weighted by the inverse of the square of the RMS computed for each SRF. Before determining the average SRF, all measurements were corrected for the change of responsivity in orbit (a decrease of 6% from start to end, Blommaert 1998 [4]). This correction reduced the overall rms ϵ (see below) from 4% to 3%. The observations divided by their input spectra are shown in Figure 11.

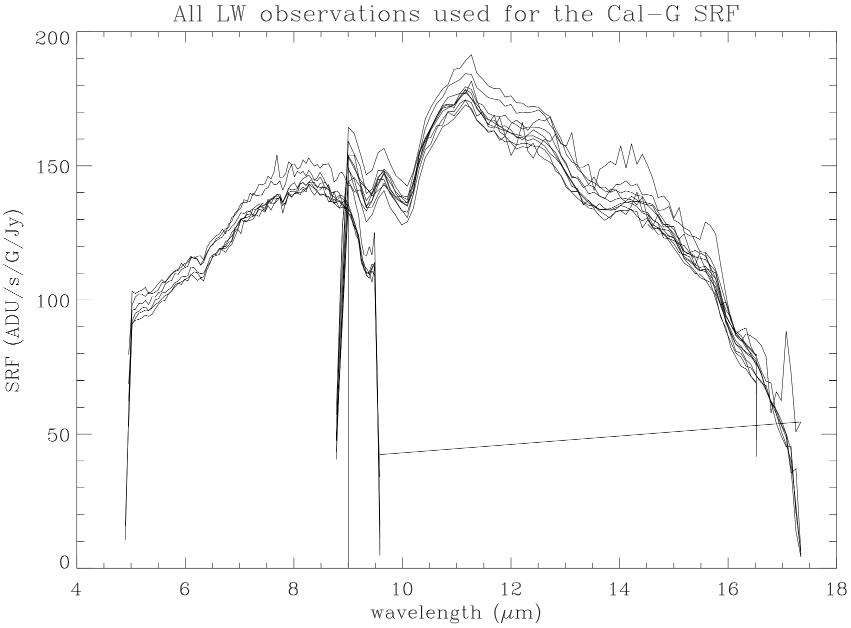

Figure 11: The different SRF determinations based on the observations of 4 different calibration stars. It includes different PFOV measurements. The RMS is 3-4 %.

5.1 Error estimate

For a given observation at each wavelength the rms of the aperture photometry is computed based on the rms of the image averaged over several frames. The rms σ_i of the SRF f_i derived from one observation of index i is computed by :

$$\sigma_i = \frac{\sigma_\phi}{m} + \frac{\phi}{m^2}\sigma_m$$

where ϕ is the in-band flux, σ_ϕ is the rms of ϕ, m is the spectral energy density value of the model and σ_m is the rms of m. The values of σ_i computed for different observations are relatively small compared to the dispersion observed among them. The error ϵ on the SRF averaged over all the valid observations is then computed by :

$$\epsilon = \sqrt{\frac{\sum[(f_i - < f_i >)/\sigma_i^2]}{\sum 1/\sigma_i^2} + \frac{1}{< 1/\sigma_i^2 >}}$$

5.1.1 Sources of the scatter in the SRFs

The typical RMS σ_i of the photometry per CVF step for a given observation is 2%. The only source which has a significantly higher RMS is HIC96441 which has a 7% RMS in CVF2. However, because of its' higher uncertainty it contributes little in the final SRF (see Section 5). The final RMS ϵ per CVF step of the SRF (based on almost 10 measurements) is about 3%. This higher value can be caused by several factors. The first uncertainty which enters the determination of the average SRF is the use of different sources with different flux densities. The different flux levels will lead to differences in stabilization which may not be perfectly

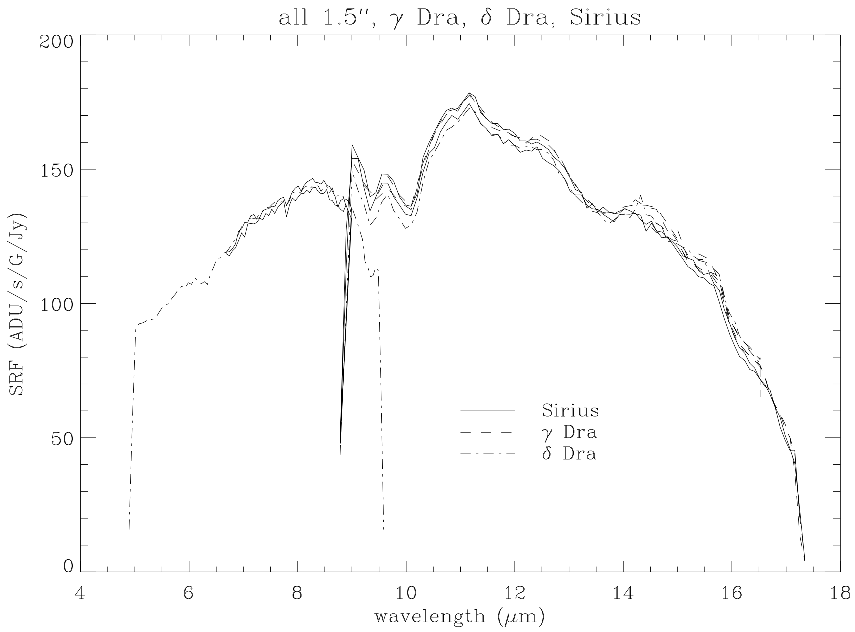

Figure 12: SRF measurements with 1.5″ PFOV.

corrected by the Fouks-Schubert method (see Section 2.1). This would mostly affect the start of the measurement. The use of different stellar models is another important aspect. The input spectra from Cohen and Decin for γ Draconis, δ Draconis and Sirius are better than 2%. The agreement for the three stars is excellent as can be seen in the plot where the SRFs measured with PFOV 1.5″ are shown (Figure 12). The GBPP model for HIC096441 claims an uncertainty of 3%. In Figure 13 the SRF for HIC096441 is too high by about 4% for CVF1. The CVF2 part has a lower S/N and is more difficult to judge. As we have no further measurements of the source it is difficult to judge the quality of the stellar model for HIC096441. Possibly the most important effect which increases the dispersion is the use of different lenses. It is clear that larger PFOV can lead to slightly higher total signals as can be seen in Figure 15. The differences can be partially explained by the differences in stabilization (more signal concentrated in fewer pixels for larger pixels and thus a faster stabilization). The main differences are however likely to come from the different apertures used (see Section 3.2.2).

5.2 Comparison with the previous SRF

In Figure 16 the ratio is shown of the *OLP v7* and *OLP v10* SRFs. The SRFs are determined on basically the same set of observations. We have used different stellar input models, but the differences in the model spectra are small (see Section 4). There are overall small differences in the SRF on the level of a few percent as can be seen in Figures 17 and 18. The main reason for this is the fact that the final SRF obtained for *OLP v7* was smoothed (Biviano et al. 1998 [2]). This was done in order to reduce noise features. The disadvantage of that method is that real spectral features in the SRF, like at around 6.3, 6.9, 9.3 and 10μm were smoothed out. The deviation seen in wavelengths above 16μm is most likely due to the different processing for the transient. We applied the Fouks-Schubert correction which was not available in the previous

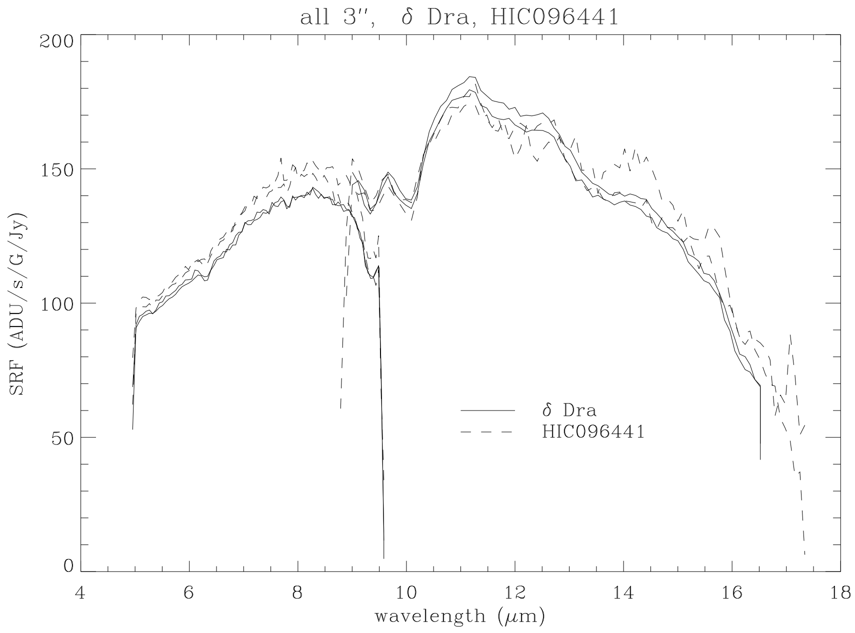

Figure 13: SRF measurements with 3″ PFOV.

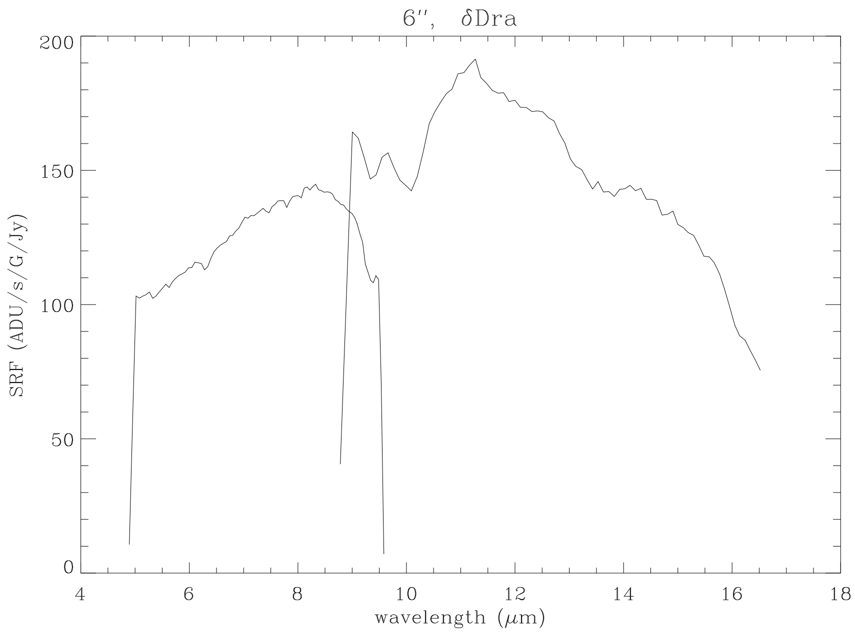

Figure 14: SRF measurement with 6″ PFOV. There is only one source measured.

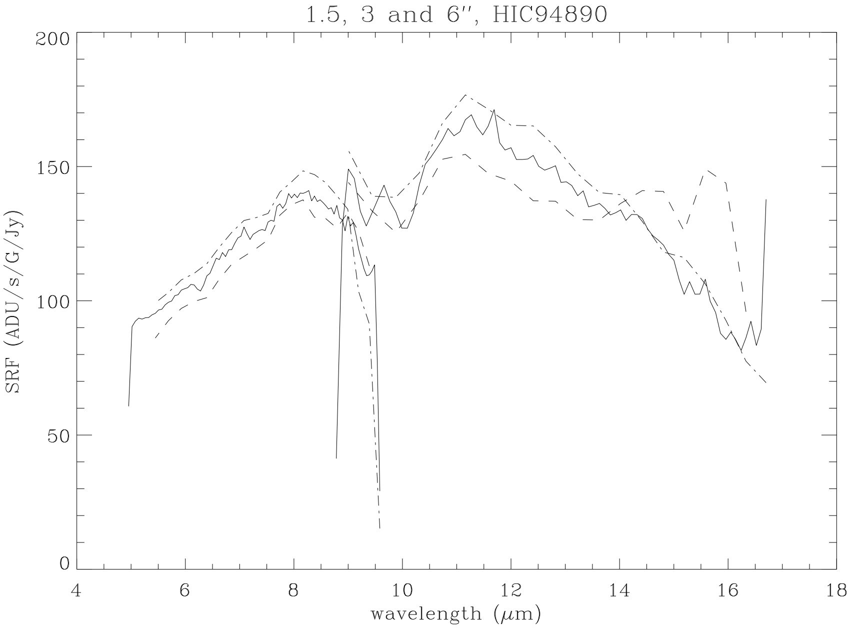

Figure 15: CVF measurements on HIC94890 performed on Rev. 58. Three different PFOVs were used. In this data set the SRF increases by 5% globally by going to the larger subsequent PFOV. The larger uncertainty at the longest wavelengths is caused by lower signals and problems in the stabilization.

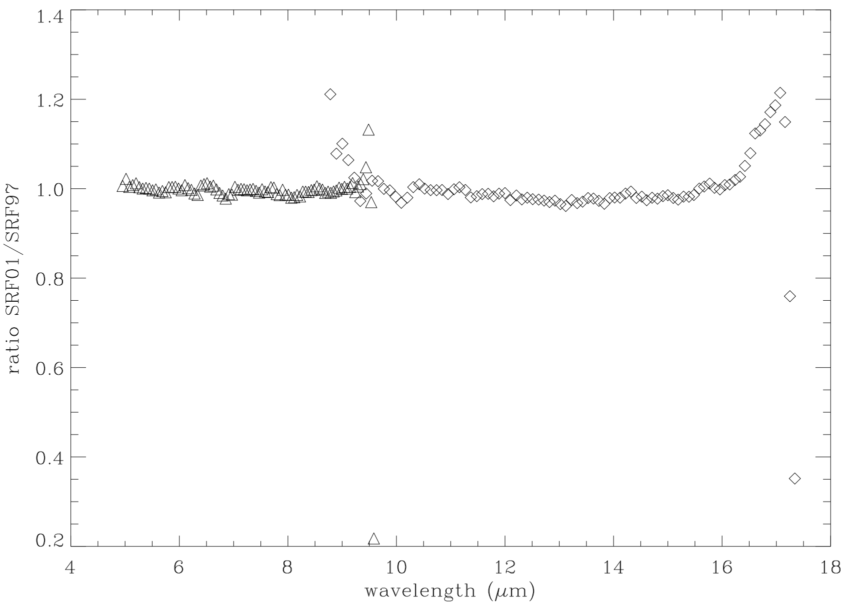

Figure 16: Comparison of the SRFs provided in OLP7 and the one for OLP10. Main differences are at the edges of the CVF segments. There are also small features at a few percent level which were not present in the OLP7 as the SRF was smoothed in order to reduce the noise.

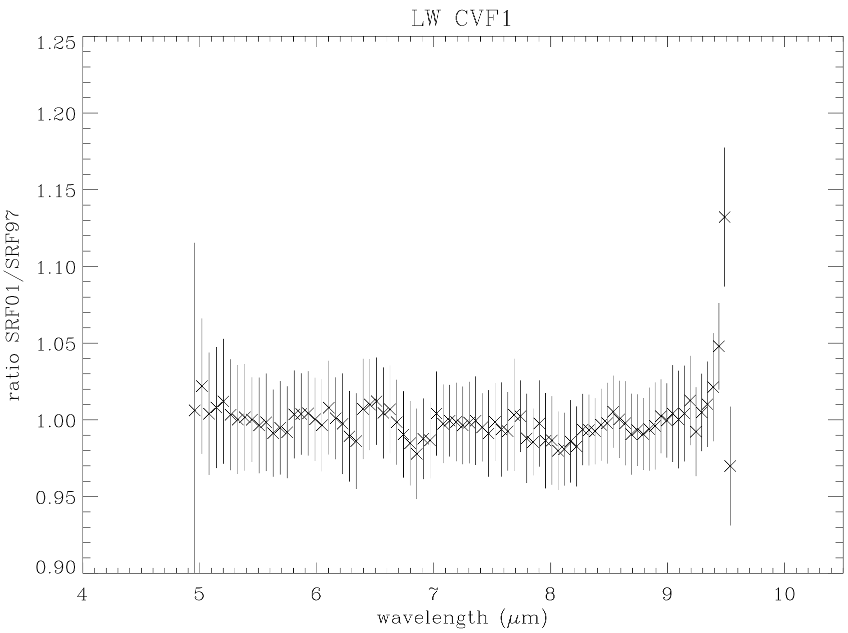

Figure 17: Like Figure 16, but for CVF1 and at a smaller scale. Spectral features can be seen which were smoothed out in the OLP7 version.

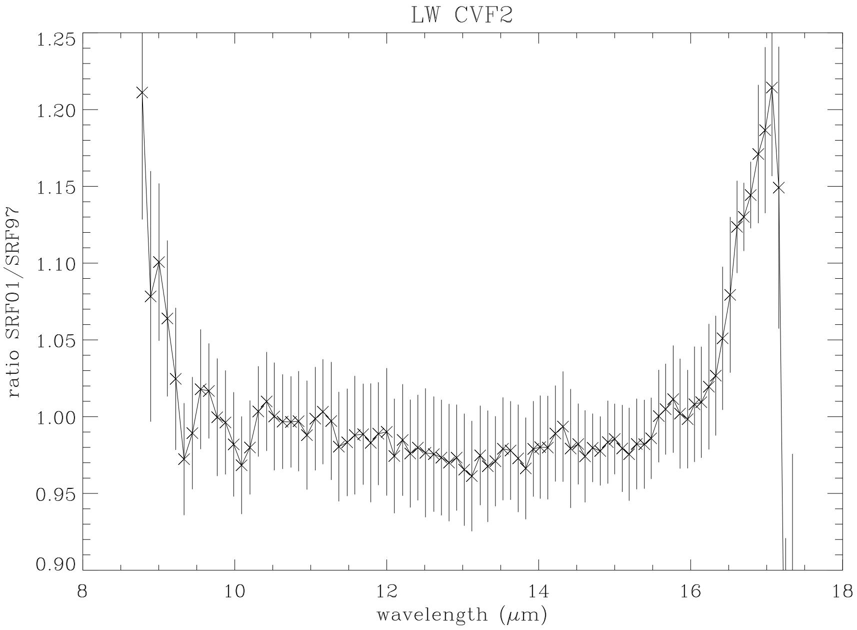

Figure 18: Like Figure 16, but for CVF2 and at a smaller scale. Spectral features can be seen which were smoothed out in the OLP7 version.

SRF determination.

6 Extended source calibration

In high latitude regions where the cirrus emission is faint, the mid-infrared sky brightness is dominated by zodiacal emission from interplanetary dust (Galactic/zodiacal emission $\sim$ 1%). For observations of high latitude in faint cirrus regions, the mid-IR sky emission is smooth and the sky brightness measured by ISOCAM, within its 3' field of view can be compared with the infrared sky survey carried out with the Diffuse Infrared Background Experiment (DIRBE) at 40' angular resolution. This opens the possibility to test the validity for extended sources of the stellar calibration.

We have performed such a comparison for a number of CVF and filter observations listed in Tables 3 and 4. Most of the CVF observations are not specific calibration data but observations in the direction of faint point like galaxies which permit to measure the foreground sky brightness around the source. For a given observation, one ISOCAM brightness is computed from the mean flux over the non-vignetted part of the camera divided by the pixel area in ADU/G/s/sr and converted to Jy/sr with the SRF based on the stellar observations, discussed in this report. The zodiacal light flux estimates where derived from the model of Kelsall 1998 [17]. The model parameters were fitted in order to reproduce the DIRBE broad-band measurement of the zodiacal light including three mid-IR wavelengths 4.9, 12 and 25μm. Its accuracy at these wavelengths, within the range of solar elongation used by both ISO and DIRBE, is estimated to be of the order of a few %. The details of the spectral dependence of the zodiacal light, in particular the plausible existence of silicate emission bands, are poorly constrained by the DIRBE data. The Kelsall et al. model is thus based on simple assumptions about the emissivity of interplanetary dust which can be tested by ISOCAM observations. In Table 5 we list the Galactic coordinates (l, b), ecliptic coordinates with the sun as the longitude reference (λ, β) and the solar elongation e of the observations used in this analysis together with the Galactic sky brightness at 100μm. For the mean high latitude dust emission spectrum $I_\nu(12\mu\mathrm{m})/I_\nu(100\mu\mathrm{m}) = 0.045$.

6.1 Filter observations

Fig. 19 shows the mean ratio between ISOCAM flux densities and the Kelsall et al. model for diverse ISOCAM filters and pixel field of views. The model flux densities were inverse colour corrected to comply with the ISOCAM photometry convention of νF_ν =Constant. All data points are scattered within 10% of 1 except for one short wavelength point (LW4) which is noisy (dark uncertainties become important with respect to expected zodiacal light brightness at the shortest ISOCAM wavelengths) and three points with the 12" pixel which are slightly above 1.1. This good agreement for filter observations between ISOCAM and DIRBE zodiacal fluxes is quite satisfactory. Uncertainties in the spectral dependence of the zodiacal emission, in the ISOCAM calibration and in the photometric accuracy of ISOCAM measurements (limitations in our understanding of long term gain variations with illumination) can all contribute to the observed scatter and it is difficult to disentangle the respective contributions. In general, the flux uncertainty of one observation computed from the RMS map of ISOCAM data is small compared to the RMS computed from a set of independent observations. In all the following figures the error bar is computed as the square root of the sum of these two types of RMS squared. The RMS of a set of independent observations is not divided by the square root of

Table 3: CVF Scans

TDT	l	b	λ	β	e	I_{100}(MJy/sr)	Direction
PFOV 6"							
06600401	306.5	53.8	256.8	-2.4	103.2	3.6	Down/Up
40701609	52.0	54.8	303.8	49.8	68.9	2.0	Down
44300306	25.0	60.5	263.3	34.7	95.5	2.4	Down
44500404	77.3	60.5	243.8	56.8	104.0	2.0	Down
44900103	317.2	54.4	245.0	1.3	115.0	3.2	Down
74601150	15.34	-57.33	78.1	-20.2	78.8	1.7	Down/Up
75301220	86.52	31.16	4.2	81.4	81.4	2.9	Down/Up
75600102	306.55	-45.99	55.7	-61.5	74.4	2.5	Down/Up
75600617	277.97	-42.81	97.5	-76.9	91.7	3.3	Down/Up
75601447	255.31	-41.42	152.7	-69.4	108.2	1.4	Down/Up
75901029	55.43	-75.89	89.9	-18.8	89.9	2.0	Down/Up
75901126	21.10	-77.22	85.9	-25.9	86.3	1.8	Down/Up
76301335	224.90	-71.80	114.1	-39.9	108.3	1.7	Down/Up
78000914	208.64	-63.14	109.6	-36.3	105.7	2.3	Down/Up
78100808	326.74	-85.55	73.3	-32.6	76.0	1.9	Down/Up
78600205	13.20	-85.02	66.6	-29.1	69.7	1.9	Down/Up
78600332	100.53	-70.21	73.7	-10.1	73.9	3.3	Down/Up
79501444	188.39	-37.98	119.7	-19.3	117.9	15.6	Down/Up
80201638	220.54	-60.99	88.8	-42.1	89.1	1.7	Down/Up
81300411	159.97	-54.15	77.1	-10.2	77.3	2.8	Down/Up
81701141	167.24	-23.79	100.9	3.4	100.9	12.22	Down/Up
86900323	34.10	13.44	260.6	30.5	98.1	13.04	Down/Up
PFOV 12"							
52901131	96.4	29.3	324.9	89.5	89.6		Down/up
61100811	164.0	-33.1	296.6	0.3	63.4		Down/Up
66100313	164.0	-33.1	248.7	0.3	111.3		Down/Up

Table 4: Observations with filters and CVF fixed positions

TDT	PFOV	Filters and CVF wavelengths
06600402	6	CVFLW11.25, LW8
41204702	12	LW3
41204904	12	LW9
41205308	12	LW2
41205510	12	LW10
46104201	6	CVFLW15.0, CVFLW11.37, CVFSW7.69
46104201	3	CVFLW15.0, CVFLW11.37, CVFSW7.69
46104201	1.5	CVFLW11.37
46104302	6	LW9, LW8, LW6
46104302	3	LW9, LW8, LW6
46104302	1.5	LW8
46104403	12	CVFLW15.0, CVFLW11.37, CVFSW7.69, LW9, LW8, LW6
52901132	6	LW7, LW8, LW6
61100812	6	LW7, LW8, LW6
66100314	6	LW7, LW8, LW6
73000402	6	LW3, LW10, LW7, LW8, LW9
73000503	6	LW3, LW10, LW7, LW8, LW9, LW2, LW1, LW4, LW5, LW6
77200501	6	LW10, LW3, LW9, LW7, LW8, LW2, CVFLW16.5, CVFLW12.0, CVF2LW9.0, CVF1LW9.0
77200602	3	LW8, CVFLW12.0
77200703	12	LW9, LW7, LW8, CVFLW16.5, CVFLW12.0, CVF2LW9.0, CVF1LW9.0

Table 5: SKY Positions for Filter Observations

Rev	l	b	λ	β	e	I_{100}
066	306.5	53.8	256.8	-2.4	103.2	3.6
412	148.0	-47.3	112.2	0.0	112.2	4.6
461	155.34	-37.25	73.6	3.2	73.7	4.1
529	96.4	29.3	324.9	89.5	89.5	3.4
611	164.0	-33.1	296.6	0.3	63.4	4.4
661	164.0	-33.1	248.7	0.3	111.3	4.4
730	88.0	37.4	350.2	79.7	79.8	1.8
772	80.24	-59.19	78.3	0.0	78.3	3.6

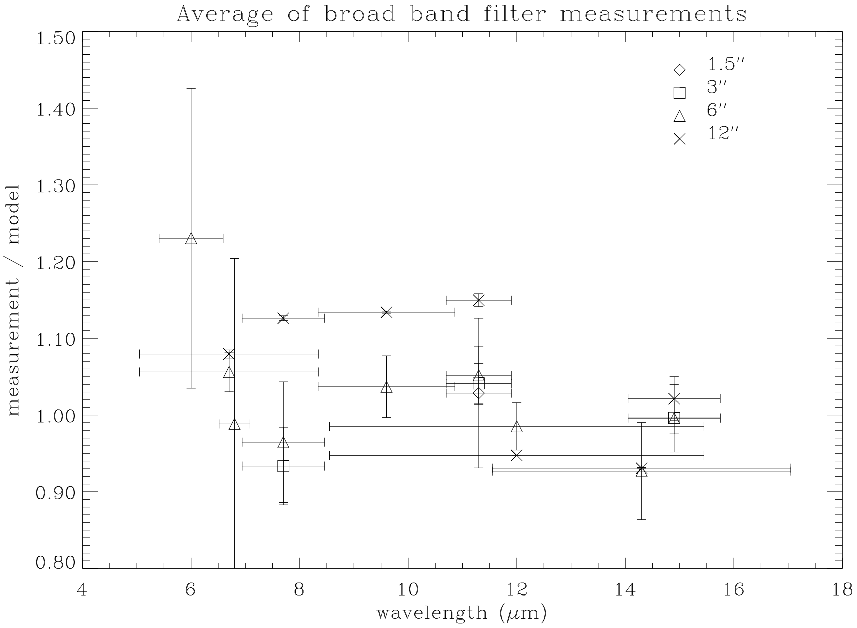

Figure 19: Mean ratio between ISOCAM and DIRBE Zody model for the set of filter observations in regions of low background cirrus emission performed downward and upward of wavelength (see Table 4). The comparison between filters and CVFs shows that the CVF photometry is affected by spectrally dependent stray light.

the number of pixels, so that the error bar indicates rather the scatter from the mean value. The uncertainty on the mean value is thus smaller than the error bar in the figures. In some configurations where only one observation is available, the error bar represents only the value derived from the RMS map which is quite small.

6.2 CVF observations

The results for the CVF observations (Fig. 21 and Fig. 22) are less satisfactory than for the filters due to multiple reflections between the ISOCAM detector and CVF. The CVF ISOCAM images of the zodiacal light obtained after flat-field corrections are not flat: they present two lung-shaped bumps to the left and right sides of the detector (Fig. 20). The reflections do not only distort the image, they also affect the calibration by bringing additional flux onto the detector. In the stellar calibration we were careful in separating spatially the ghosts from the main image. Since this spatial separation is obviously not possible for extended sources, the additional flux brought by the reflections is included in the zodiacal brightness measurement but excluded in the stellar calibration ISOCAM. This explains why the two curves in Figs. 21 and 22 are systematically above 1. This figure also shows that the amplitude of this effect onto extended source calibration varies significantly with wavelength and thus affects not only the overall flux calibration but also the shape of the spectra. The curves in Figs. 21 and 22 differ only by a small offset within plausible uncertainties on the actual value of the dark current level. The comparison of these curves show that the ISOCAM/DIRBE comparison is quite uncertain below 8μm due to uncertainties on the dark current.

The error bars in Fig. 21 represent the RMS dispersion of the individual measurements used to derive the mean curve. The full histogram of the value at 12 μm is shown in Fig. 23. This

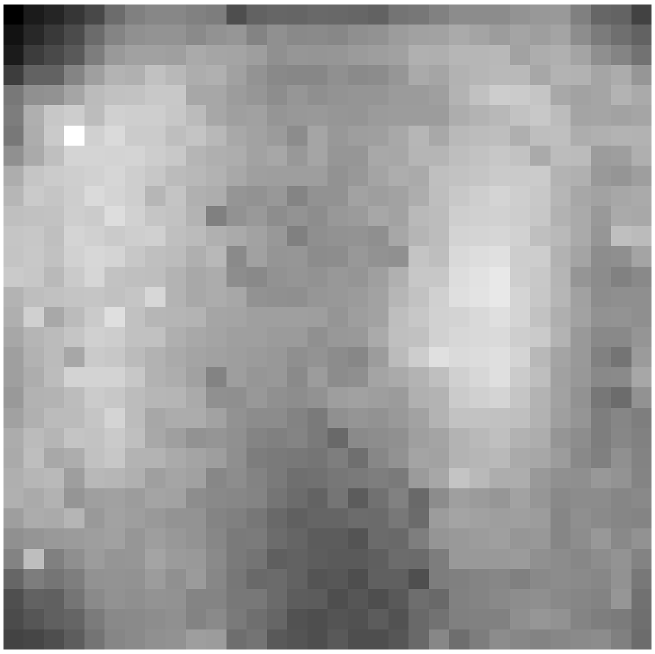

Figure 20: So-called two-lung shaped ghosts in e flat extended source

figure illustrates the good reproducibility of the ISOCAM photometry within a given observing mode. The correlation between the ISOCAM to model ratio and the solar elongation show that part of the scatter is not instrumental but represents the detection of real departures from the model (Fig. 28).

The "down" and "up" curves disagree by more than the dispersion of the individual measurements for a given scanning direction. This is the residual memory effect which is not fully corrected by the current transient correction algorithm. Note that at longer wavelengths, the dispersion is higher in the "down" curve. The memory effect related to the past illumination is never well corrected because we do not know the complete detector history.

6.3 Proposed correction of straylight

Our understanding of the CVF observations of the zodiacal emission can be summarized in the following formula:

$$\text{CVF Observation Cube} = \text{True Zody Spectrum}(\lambda) \times (1 + S(\lambda) \times \text{Stray Cube})$$

where Stray cube is a set of images of the spatial distribution of the stray emission as a function of CVF wavelength step. In this formula the stray cube is normalized to 1 over the central part of the CAM array (pixels 10 to 21) and $S(\lambda)$ is the normalization factor, i.e. the mean amplitude of the stray emission as a function of wavelength.

The CVF stellar observations permit to correct for the spectral dependence of the stray light (i.e. the $S(\lambda)$ term in the above equation) within the assumption that it is independent of the source position. We have used observations where the ghost was well displaced from the main star image to estimate the spectral dependence of its relative amplitude. (Fig. 25 and § 3.2.3 for more details). Fig. 26 shows the ratio of the CVF to zodiacal model after correction by

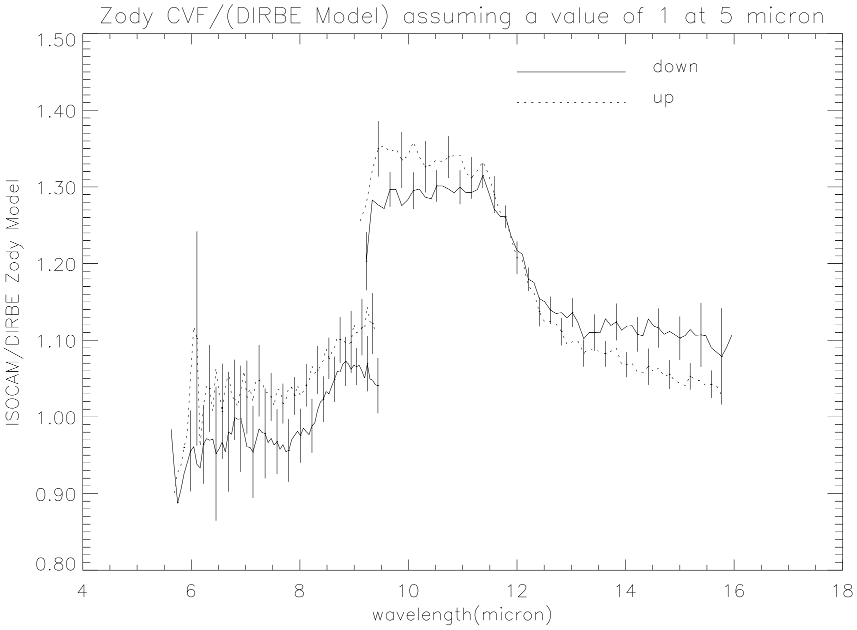

Figure 21: Mean ratio between CVF spectra and DIRBE Zody model for the set of 14 observations in regions of low background cirrus emission done down and up in wavelength with the 6" lens (see Table 3). The error bars represent the RMS dispersion of the individual measurements used to derive the mean curve. Note that due to the systematic memory effect, the "down" and "up" curves disagree by more than the dispersion of the individual measurements for a given scanning direction. An offset correction was applied to each observation before transient correction in order to have ISOCAM/DIRBE ratio of unity at 5 μm. The mean offset is 0.1 ADU/s/g with RMS scatter of 0.03.

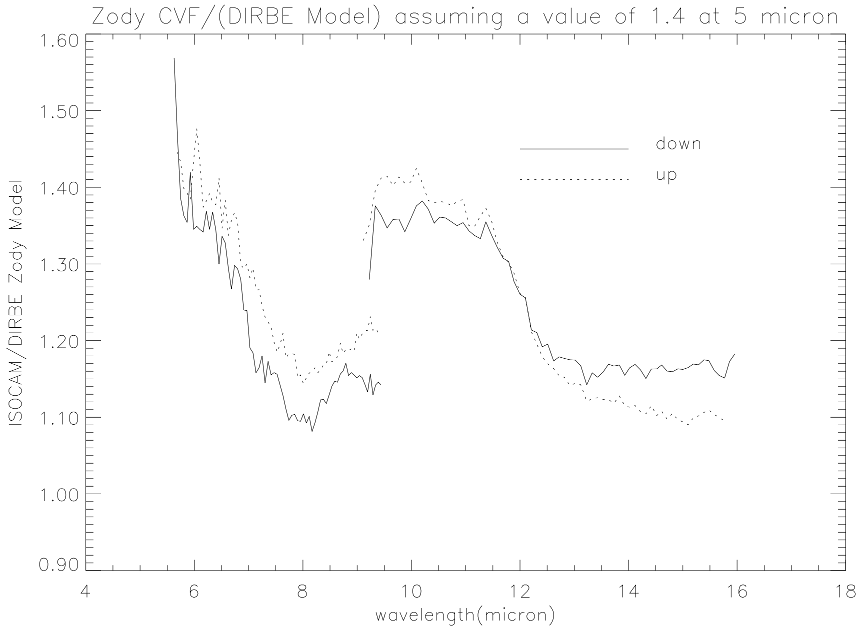

Figure 22: Mean ratio between CVF spectra and DIRBE Zody model for the same set of observations as in Figure 21. The only difference with Figure 21 is that the offset correction was determined in order to have ISOCAM/DIRBE ratio of 1.45 at 5 μm. The mean offset is 0.23 ADU/s/g with RMS scatter of 0.08. The comparison between this and the previous figure shows the impact of uncertainties on the dark current on these curves.

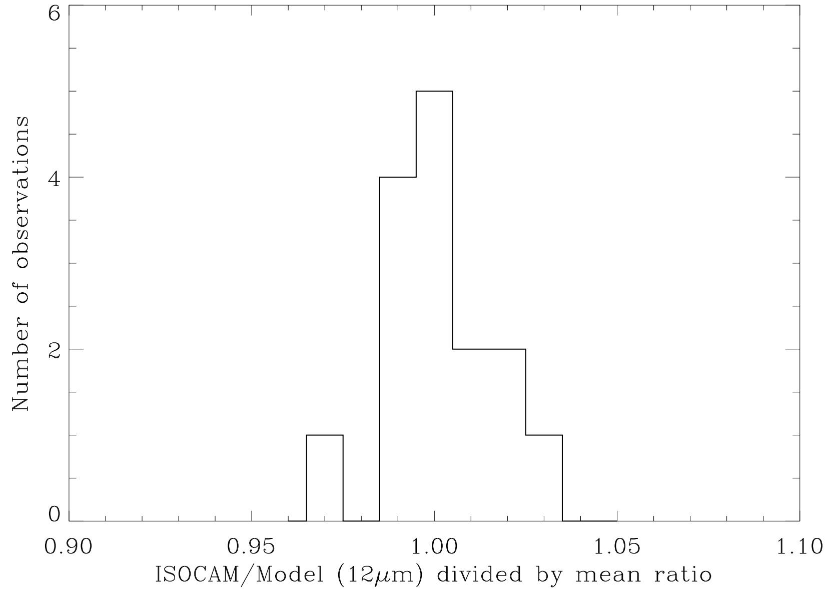

Figure 23: Histogram showing the full distribution of the ratio at 12 μm between the CVF and the model. The values for the different observations have been divided by the mean value. All measured values are within 3% from the mean value. This illustrates the good reproducibility of the ISOCAM photometry within a given observing mode.

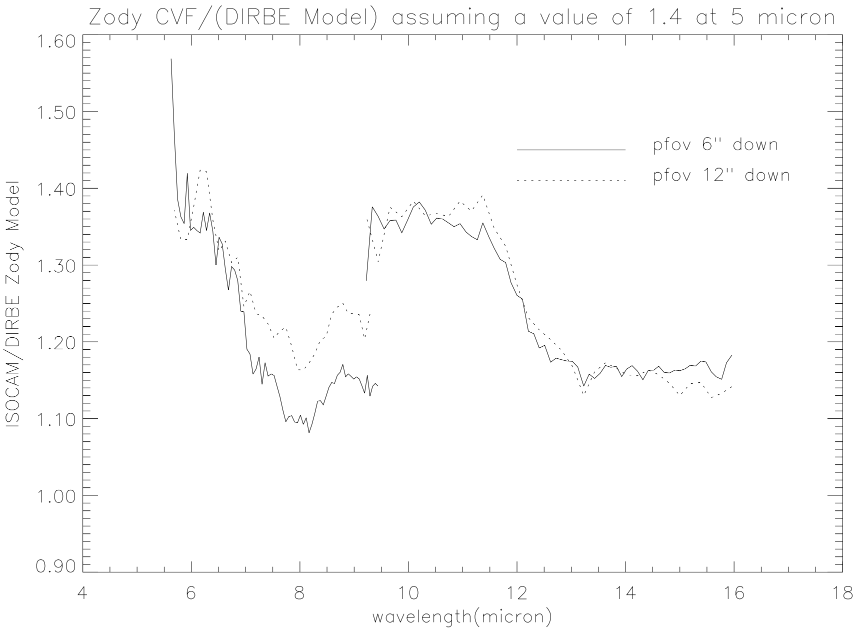

Figure 24: Mean ratio between ISOCAM CVF and DIRBE zody model for 6 and 12" lens. Both curves are for scans going down in wavelength. In both cases we have made a dark correction so that the ISOCAM/DIRBE ratio is for each observation 1.45 at 5 μm. The dark correction is 0.23 ADU/G/s and 0.15 ± 0.07 ADU/G/s for the 6 and 12" spectra respectively.

this determination of the stellar ghost amplitude. This correction brings the CVF in agreement with the filter data points. This is a quite satisfactory result which give us confidence in the assumption made in extrapolating the measurement at one source position to the whole camera field of view. The spectral dependence left in the CVF data could represent a real spectral dependence of the zodiacal emission not taken into account in the Kelsall et al. model. This feature cannot be instrumental, because its strength depends in a systematic way on the solar elongation (Fig. 28). The high amplitude of ghosts found for the stellar observations at short wavelengths is found for the zodiacal CVF only when we add an offset of 0.23 ADU/G/s to the raw data prior to transient correction (curves in Fig. 22). The amplitude of this offset correction is comparable for the 12" pfov observations while the fluxes are 4 times larger. To test it we also looked at a few dark observations. An offset correction of comparable amplitude was necessary to have a flux at dark equal to zero after transient correction (Fouks-Schubert method). In the absence of such a positive offset the flux at dark is negative after transient correction. The need for this correction seems to follow from the fact that the *official* dark correction is based on dark measurements which are non transient corrected. Thus, the official dark level is contaminated by the memory effect from the past illumination. Further, the dark determination ignores a possible non-zero stray illumination of the detector in the dark current measurement configuration.

The simple fact that the images of stray light are not flat shows that the stray light amplitude does depend on position and thus that the assumption made above is not fully valid. We have tried to take the spatial dependence in account in the following way. The stray light amplitude measured with the point source is not anymore assumed to represent the mean value over the central part of the CAM array but instead the mean value within a small area around the point source position. The stray light intensity in the central region is computed from this position in the following way. Assuming that the zodiacal light observation cube I is decomposed into uniform term z (True Zody Spectrum in the previous formula) and a ghosts contribution G which depends on the wavelength and the position on the detector ($S(\lambda)\times$ Stray Cube in the previous formula).

$$I(i,j,\lambda) = z(\lambda)(1 + G(i,j,\lambda))$$

The ghosts contribution G is computed from the relation:

$$\frac{I(i,j,\lambda)}{< I(a,b,\lambda) >} = \frac{1 + G(i,j,\lambda)}{1 + < G(a,b,\lambda) >}$$

where $< (a,b,\lambda) >$ represents the average in the region (a,b) centered on the position (20,6) where the γ Draconis is located in the ghost measurements (see § 3.2.3). The ratio of the ghost to the zodiacal light spectrum S is then computed by averaging G in the central region : $S(\lambda) =< G(10:21, 10:21, \lambda) >$. The results of the stray light correction within this assumption are shown in Fig. 27. The only difference with the previous correction is that the ISOCAM/DIRBE CVF curve is scaled down by about 7%. The match with the filter observations is better than in the first correction at long wavelengths but worse between 8 and 12μm. The discrepancy between the CVF curve and the filter points below 8μm could be corrected by an additional dark current offset. We have not quantified the necessary correction.

The correction proposed here to correct the zodiacal spectra for the straylight radiation would apply equally well to any other source illuminating roughly uniformly the field of view of the camera. It thus applies to CVF measurements of the diffuse Galactic emission in regions where the emission has little small scale structure. But we do not see any meaningful correction to propose for the larger number of CVF observations of extended sources with contrasted structure (e.g. Photo-dissociation region).

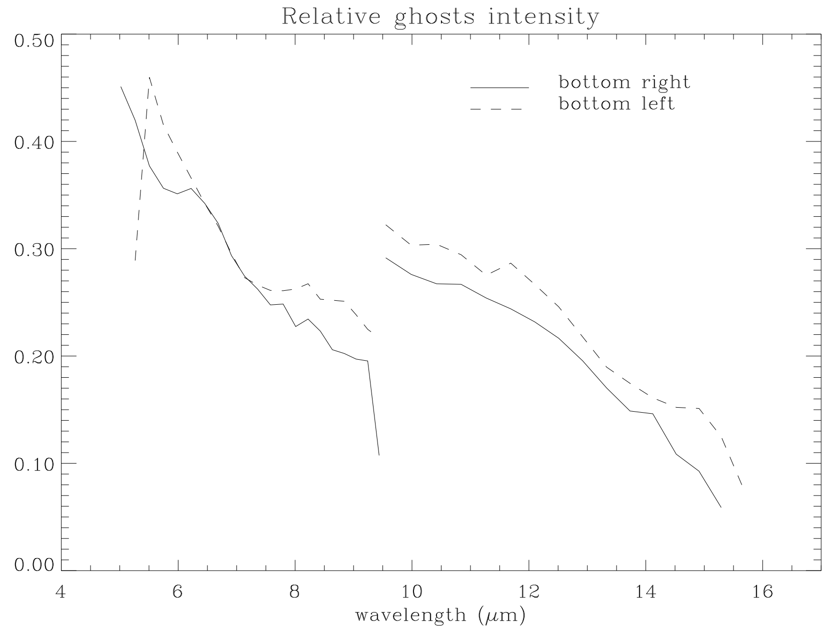

Figure 25: The summed relative intensity of the first and secondary ghosts normalized to the point source flux in the main beam at 2 positions on the detector. The comparison of this spectral dependency with that on Figs 21 and 22 suggest that a part of the spectral difference between ISOCAM and DIRBE spectra might be intrinsic to the zodiacal light.

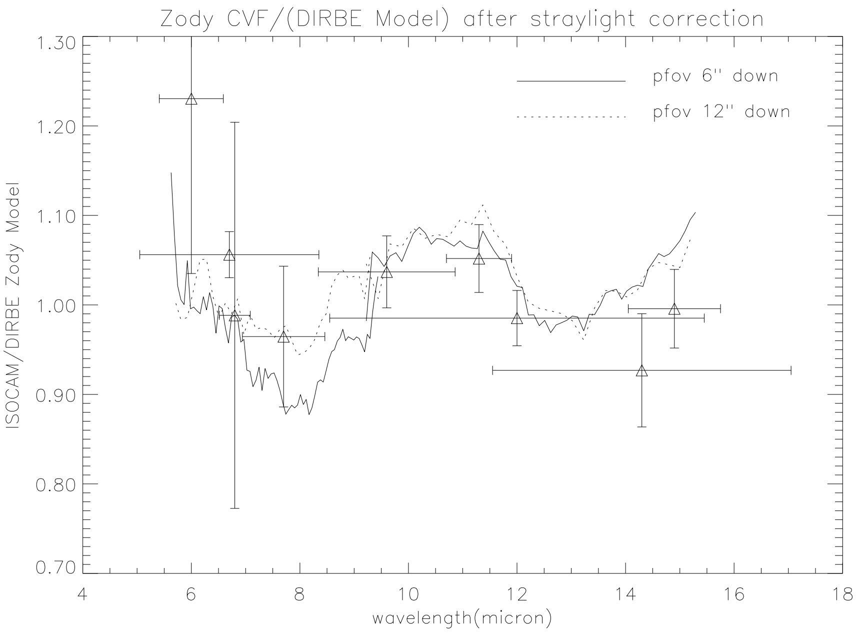

Figure 26: Mean ratio between ISOCAM and DIRBE after correction of straylight amplitude determined on point sources (see figure 24). The residual spectra obtained with the 6" lens data (solid line) and 12" lens data (dash line), both scanning down in wavelengths, are compared with the 6" lens filter measurements. We tentatively consider this residue as the ISOCAM correction to the zody spectrum in the Kelsall model.

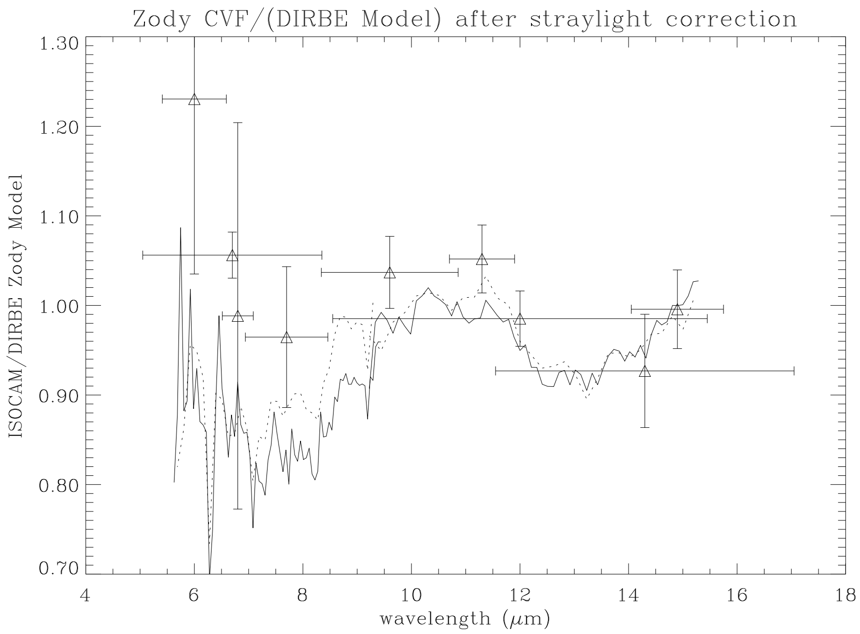

Figure 27: Same as Fig 26, but here the ghosts intensity is derived in taking into account the spatial variation of the ghosts spectrum.

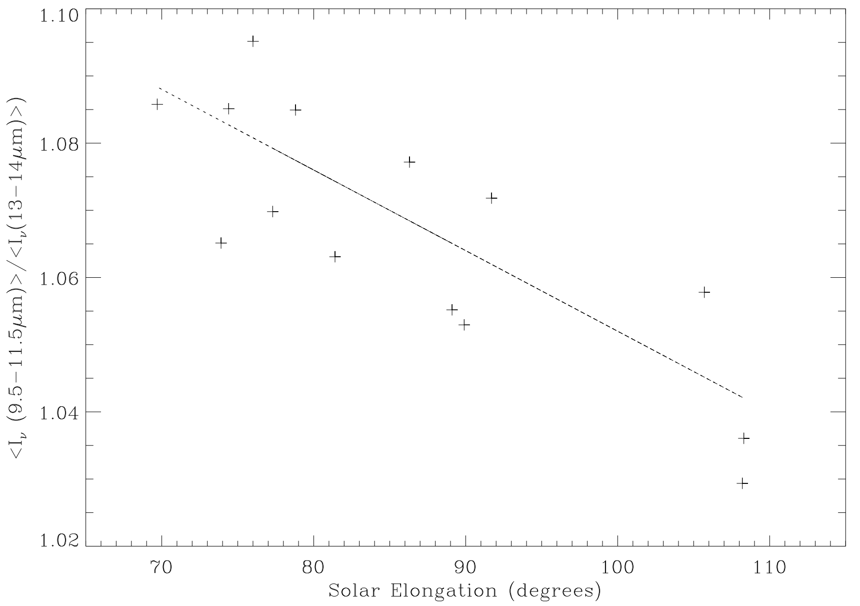

Figure 28: Strength of the purported *silicate feature* as a function of the solar elongation of the observation. The intensity of the feature has been measured by the ratio of the mean value between 9.5 to 11.5 μm and 13 to 14 μm, after normalization of each CVF spectrum by the zodiacal model and correction of the stray light.

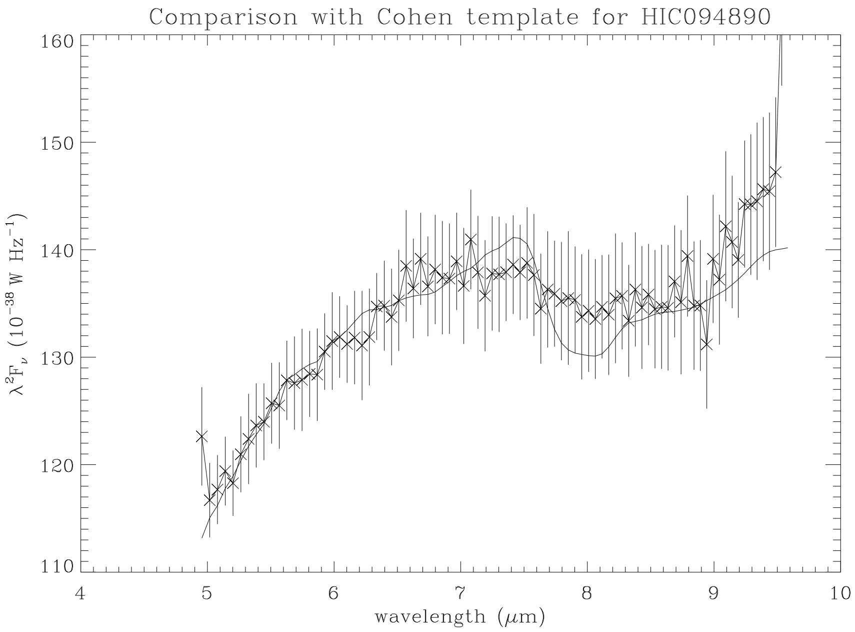

Figure 29: Comparison of the CVF spectrum on HIC 094890 with the stellar template provided by Cohen. The observation shows a stronger SiO fundamental absorption feature at 8μm.

A Comparison of the CVF with the stellar template for HIC 094890

On revolution 58, HIC 094890 was observed with the CVF. As was discussed in § 4 the measurement was not used for the determination of the SRF as the stellar template provided by Cohen is less certain in the wavelength ranges of the molecular absorption bands. Fig.29 shows the comparison of the HIC 094890 CVF1 spectrum ($1.5''$, TDT 05804903) with the stellar template provided by Cohen. The spectrum is obtained using the SRF discussed in this report. The spectrum and the template agree well up to 7μm where the SiO fundamental absorption feature starts. The observed molecular band absorption feature is deeper than seen in the stellar template. The deviation near the edge, beyond 9.5μm, is most likely caused by a problem with the stabilization at the start of the CVF measurement.

References

[1] A. Biviano, B. Altieri., J. Blommaert, F. Boulanger, D. Cesarsky, K. Okumura, W. Reach, "Topics in ISOCAM Spectroscopy Calibration". *Proceedings of the first ISO workshop on analytical spectroscopy*, 1997

[2] A. Biviano, B. Altieri., J. Blommaert, F. Boulanger, D. Cesarsky, L. Metcalfe, K. Okumura, W. Reach, "The ISOCAM CVF Calibration Report". Technical report, 1998, http://www.iso.vilspa.esa.es/

[3] A. Biviano, "The ISOCAM calibration error budget report". Technical report, 1998, http://www.iso.vilspa.esa.es/

[4] J. Blommaert, "ISOCAM photometry report". Technical report, 1998, http://www.iso.vilspa.esa.es/

[5] Photometry Working Group Report, 2001, http://www.iso.vilspa.esa.es/

[6] Cohen, Walker, Carter, Hammersley, Kidger and Noguchi, *Astronomical Journal* 117, 1864, 1999

[7] M. Cohen "Stellar calibration in the infrared: extending the legacy of the KAO, ISO and MSX to SIRTF and beyond" *Proceedings of the Conference "The Calibration Legacy of the ISO Mission"*, ESA SP-481, 2001

[8] A. Coulais and A. Abergel, "Transient correction of the LW-ISOCAM data for low contrasted illumination". *Astron. Astrophys. Suppl. Ser.* 141, 533-544, 2000

[9] L. Decin, C. Waelkens, K. Eriksson, et al., *Astronomy & Astrophysics*, 364, 137, 2000

[10] L. Decin, "Stellar models in IR calibration". *Proceedings of the Conference "The Calibration Legacy of the ISO Mission"*, ESA SP-481, 2001

[11] L. Decin, B. Vandenbussche, C. Waelkens, et al., *Astronomy & Astrophysics*, submitted, 2001

[12] P. Garcia, "ISO Cross Calibration Report", ESA Technical Report, http://www.iso.vilspa.esa.es

[13] Hammersley et al. *Astronomy & Astrophysics Supplem. Series*, 128, 207, 1998

[14] P. Hammersley, Jourdain de Muizon, M., "The development of stellar photometric standards for ISO". *Proceedings of the Conference "The Calibration Legacy of the ISO Mission"*, ESA SP-481, 2001

[15] ISOCAM Interactive Analysis User's Manual. *Edited by Delaney M., Stockholm University*, 2000

[16] ISO Handbook Volume VI: SWS - The Short Wavelength Spectrometer ESA, SAI/2000-008/Dc, 2001, http://www.iso.vilspa.esa.es/

[17] Kelsall, T. et al. "The COBE Diffuse Infrared Background Experiment Search for the Cosmic Infrared Background. II. Model of the Interplanetary Dust Cloud". ApJ 508, 44, 1998

[18] K. Okumura, "ISOCAM PSF report". Technical report, 1998, http://www.iso.vilspa.esa.es/

[19] K. Okumura, M. Pérault, Y. Longval and F. Sibille, "Ghosts in ISOCAM images". Technical report, 1998, http://www.iso.vilspa.esa.es/

[20] K. Okumura, "The ISO point spread function and CAM beam profiles". *Proceedings of the Workshop: ISO beyond point sources: study of extended infrared emission*, 47–52, ESA SP-455, April 2000

[21] K. Okumura, "Optical properties of ISOCAM and/or ISO telescope". *Proceedings of the Conference "The Calibration Legacy of the ISO mission"*, ESA SP-481, 2001